



1       Tropospheric NO<sub>2</sub> Measurements Using a Three-wavelength  
2       Optical Parametric Oscillator Differential Absorption Lidar

3           Jia Su<sup>1</sup>, M. Patrick McCormick<sup>1,\*</sup>, Matthew S. Johnson<sup>2</sup>, John T. Sullivan<sup>3</sup>, Michael J.  
4           Newchurch<sup>4</sup>, Timothy A. Berkoff<sup>5</sup>, Shi Kuang<sup>4</sup>, Guillaume P. Gronoff<sup>5, 6</sup>

5       <sup>1</sup>Center for Atmospheric Sciences, Department of Atmospheric and Planetary Sciences, Hampton  
6       University, Hampton, Virginia 23668, USA

7       <sup>2</sup> Earth Science Division, NASA Ames Research Center, Moffett Field, CA, USA

8       <sup>3</sup>NASA Goddard Space Flight Center, Chemistry and Dynamics Laboratory, Greenbelt, MD  
9       20771, USA

10      <sup>4</sup>Atmospheric and Earth Science Department, University of Alabama in Huntsville, Huntsville,  
11      Alabama, USA

12      <sup>5</sup>NASA Langley Research Center, Hampton, VA, 23681, USA

13      <sup>6</sup>Science Systems and Applications, Inc

14      Correspondence to: M. Patrick McCormick ([PAT.MCCORMICK@HAMPTONU.EDU](mailto:PAT.MCCORMICK@HAMPTONU.EDU))

15

16      **Abstract**

17      The conventional two-wavelength Differential Absorption Lidar (DIAL) has measured air  
18      pollutants such as nitrogen dioxide (NO<sub>2</sub>). However, high concentrations of aerosol within the  
19      planetary boundary layer (PBL) can cause significant retrieval errors using only a two-  
20      wavelength DIAL technique to measure NO<sub>2</sub>. We proposed a new technique to obtain more  
21      accurate measurements of NO<sub>2</sub> using a three-wavelength DIAL technique based on an Optical  
22      Parametric Oscillator (OPO) laser. This study derives the three-wavelength DIAL retrieval  
23      equations necessary to retrieve vertical profiles of NO<sub>2</sub> in the troposphere. Additionally, two  
24      rules to obtain the optimum choice of the three wavelengths applied in the retrieval are designed  
25      to help increase the differences of the NO<sub>2</sub> absorption cross sections and reduce aerosol  
26      interference. NO<sub>2</sub> retrieval relative uncertainties caused by aerosol extinction, molecular



27 extinction, absorption of gases other than the gas of interest and backscattering are calculated  
28 using two-wavelength DIAL (438 nm and 439.5 nm) and three-wavelength DIAL (438 nm,  
29 439.5 nm and 441 nm) techniques. The retrieval uncertainties of aerosol extinction using the  
30 three-wavelength DIAL technique are reduced to less than 2% of using the two-wavelength  
31 DIAL technique. Moreover, the retrieval uncertainty analysis indicates that the three-wavelength  
32 DIAL technique can reduce more fluctuation caused by aerosol backscattering than two-  
33 wavelength DIAL technique. This study presents NO<sub>2</sub> concentration profiles which were  
34 obtained using the HU (Hampton University) three-wavelength OPO DIAL. As a first step to  
35 assess the accuracy of the HU lidar NO<sub>2</sub> profiles we compared the retrievals to simulated data  
36 from WRF-Chem model. This comparison suggests that the NO<sub>2</sub> profiles retrieved with the  
37 three-wavelength DIAL technique have similar vertical structure, and magnitudes typically  
38 within  $\pm 0.1$  ppb, of modeled profiles.

## 39 **1. Introduction**

40 Nitrogen dioxide (NO<sub>2</sub>) plays a critical role in the tropospheric chemistry and is one of reactive  
41 gases collectively referred to as “nitrogen oxides” (NO<sub>x</sub> = nitric oxide and nitrogen dioxide (NO  
42 + NO<sub>2</sub>)) [U.S. EPA, 2018]. The main emissions sources of NO<sub>x</sub> include transportation (on-road  
43 vehicles, airplanes, trains, ships), wood burning, industrial and chemical processes, activities for  
44 oil and gas development, soil emissions, lightning and wildfires (see Nitrogen Oxides Emissions  
45 indicator) [U.S. EPA, 2018]. Once emitted, NO reacts rapidly in the presence of ozone to form  
46 NO<sub>2</sub>. In U.S. urban locations, most measured airborne NO<sub>2</sub> comes from the reaction of these two  
47 precursors, rather than from direct NO<sub>2</sub> emissions [Bertram, et al., 2005; Beirle, et al., 2011].  
48 Scientific evidence indicates that short-term NO<sub>2</sub> exposure, ranging from 30 minutes to 24 hours,  
49 can cause the exacerbation of asthma symptoms, in some cases resulting in hospitalization



50 [Berglund, et al., 1993]. Long-term NO<sub>2</sub> exposure is likely to have a causal relationship with  
51 respiratory effects, based on evidence for the development of asthma [U.S. EPA, 2016]. And  
52 NO<sub>2</sub> will be included in future cycles of the Global Burden of Disease as global exposure  
53 estimates and evidence on their role as independent risk factors accumulates [Larkin et al., 2017].  
54 Additionally, atmospheric processing of NO<sub>2</sub> leads to the formation of nitrogen-bearing particles  
55 that can eventually deposit to the surface, causing acidification, nitrogen enrichment, and other  
56 ecological effects [Russell et al., 2012]. Local or global NO<sub>2</sub> monitoring is essential for  
57 understanding atmospheric chemistry as well as for human-health and environmental  
58 management and control.

59 Measurements of the intensity of ultraviolet or visible absorption spectra from the ground or  
60 from satellites are commonly used to retrieve the column density of NO<sub>2</sub> [Celarier et al., 2008;  
61 Valks et al., 2011; Berg et al., 2012]. Satellite-based instruments such as Ozone Monitoring  
62 Instrument (OMI), Global Ozone Monitoring Experiment (GOME and GOME-2) and SCanning  
63 Imaging Absorption SpectroMeter for Atmospheric CHartographY (SCIAMACHY) can provide  
64 global scale NO<sub>2</sub> column measurements during daytime [Boersma et al., 2008; Bucsela et al.,  
65 2008] . However, they are unable to track local anthropogenic emissions due to their long repeat  
66 cycle and large footprints, since the lifetime of tropospheric NO<sub>2</sub> is only about 6 hour in summer  
67 and 18-24 hours in winter due to photochemical effect [Beirle, et al., 2003; Cui et al., 2016]. In  
68 addition, measurements of tropospheric NO<sub>2</sub> from satellite or aircraft are also influenced and  
69 limited by clouds [Bovensmann et al., 1999; Liang et al., 2017]. Ground-based measurements of  
70 column NO<sub>2</sub> from instruments such as Pandora using differential optical absorption spectroscopy  
71 (DOAS) are often used for the validation of satellite instruments [Herman et al., 2009; Lamsal et  
72 al., 2014; Kollonige et al., 2018]. In situ measurements of near-surface NO<sub>2</sub> can best monitor



73 local emissions. However, at this point in time, they cannot provide vertically-resolved  
74 measurements. Balloon measurements using a NO<sub>2</sub>-sonde can produce vertical profiles, but these  
75 measurements are very limited in time and space, especially in the Southern Hemisphere. The  
76 primary source of data on the vertical distribution of NO<sub>2</sub> comes from operational sites around  
77 the world. However, their operation can be expensive and labor-intensive. [Scott et al., 1999;  
78 Herman et al., 2009].

79 The DIAL technique offers the potential for autonomous, 24-7 operation, with improved  
80 temporal resolution. Absorption of light by molecules is the basis for DIAL and numerous  
81 atmospheric constituents absorb light. Conventional DIAL operates at two absorption  
82 wavelengths, one stronger than the other indicated by on ( $\lambda_{on}$ ) and off ( $\lambda_{off}$ ) wavelength of the  
83 gaseous absorption feature of interest. Because of different absorption at  $\lambda_{on}$  and  $\lambda_{off}$ , the  
84 difference between the backscattered laser signals at the two wavelengths can be used to derive  
85 the number density of the absorption gas. Taking the log-ratio of these returns at closely spaced  
86 wavelengths removes system parameters and attenuation to and from the target of interest [Rothe  
87 et al., 1974; Sullivan et al., 2014]. Thus, this technology provides measurements of the quantity  
88 of gas, such as NO<sub>2</sub>, O<sub>3</sub>, and SO<sub>2</sub> at a particular location and time [Fredriksson et al., 1984;  
89 Newchurch et al., 2003; Kuang et al., 2013; Sullivan et al., 2017]. The DIAL technique provides  
90 the unique capability of remotely monitoring urban/rural area localized NO<sub>2</sub>  
91 concentrations/emissions and profiling their tropospheric vertical NO<sub>2</sub> concentration. However,  
92 aerosols are abundant within the PBL and can cause significant retrieval errors in a two-  
93 wavelength DIAL technique to measure NO<sub>2</sub>. To better understand this aerosol problem and  
94 produce a more accurate NO<sub>2</sub> profile measurement, we described a new technique using a three-  
95 wavelength DIAL technique based on the intrinsic capabilities of using a multi-wavelength OPO



96 laser system. HU has incorporated an OPO laser into its lidar system. The OPO laser enables  
 97 researchers to optimize (tune) wavelength choices for specific measurements [P.Weibring et al.,  
 98 2003]. The three-wavelength DIAL retrieval equations are derived in this study. Our optimum  
 99 choices for the three wavelengths to be used for our NO<sub>2</sub> retrievals are designed to help increase  
 100 the difference in NO<sub>2</sub> absorption cross section, and reduce aerosol influence. NO<sub>2</sub> retrieval  
 101 relative uncertainties are calculated using the two-wavelength DIAL (438 nm and 439.5 nm) and  
 102 the three-wavelength DIAL (438 nm, 439.5 nm and 441 nm). Tropospheric NO<sub>2</sub> profiles were  
 103 obtained by applying the proposed technique to HU OPO DIAL lidar. As a first-order assessment,  
 104 the HU lidar results were compared with simulated data from the WRF-Chem air quality model.

## 105 2. Method

106 To minimize aerosols-interference on the retrievals of NO<sub>2</sub>, a three-wavelength DIAL technique  
 107 was proposed with  $\lambda_1 < \lambda_2 < \lambda_3$ . Table 1 shows expressions for the extinction and backscatter of  
 108 molecules and aerosols for these three wavelengths. In Table 1,  $\beta_m$  and  $\beta_a$  are backscatter from  
 109 molecules and aerosols for the wavelength of  $\lambda_2$ ;  $\alpha_m$  and  $\alpha_a$  are the extinction of molecules and  
 110 aerosols for the wavelength of  $\lambda_2$ ;  $e$  is the aerosol Ångström exponent and assumed to be equal  
 111 for the three wavelengths because the three wavelengths are very close.

Table 1. Extinction and backscatter of molecule and aerosol for wavelengths of  $\lambda_1$ ,  $\lambda_2$  and  $\lambda_3$ .

wavelength	Molecular backscattering	Aerosol backscattering	Molecular extinction	Aerosol extinction
$\lambda_1$	$\left(\frac{\lambda_1}{\lambda_2}\right)^{-4} \beta_m$	$\left(\frac{\lambda_1}{\lambda_2}\right)^{-e} \beta_a$	$\left(\frac{\lambda_1}{\lambda_2}\right)^{-4} \alpha_m$	$\left(\frac{\lambda_1}{\lambda_2}\right)^{-e} \alpha_a$
$\lambda_2$	$\beta_m$	$\beta_a$	$\alpha_m$	$\alpha_a$
$\lambda_3$	$\left(\frac{\lambda_3}{\lambda_2}\right)^{-4} \beta_m$	$\left(\frac{\lambda_3}{\lambda_2}\right)^{-e} \beta_a$	$\left(\frac{\lambda_3}{\lambda_2}\right)^{-4} \alpha_m$	$\left(\frac{\lambda_3}{\lambda_2}\right)^{-e} \alpha_a$

The three elastic lidar equations can be expressed as:



$$X(\lambda_1, Z) = C_1 \frac{\left[\left(\frac{\lambda_1}{\lambda_2}\right)^{-4} \beta_m(Z) + \left(\frac{\lambda_2}{\lambda_1}\right)^{-e} \beta_a(Z)\right]}{Z^2} \exp\left\{-2 \int_0^Z \left[\left(\frac{\lambda_1}{\lambda_2}\right)^{-4} \alpha_m(z) + \left(\frac{\lambda_2}{\lambda_1}\right)^{-e} \alpha_a(z) + \sigma_N(\lambda_1, z) N_N(z) + O_{abs}(\lambda_1, z)\right] dz\right\} \quad (1)$$

$$X(\lambda_2, Z) = C_2 \frac{[\beta_m(Z) + \beta_a(Z)]}{Z^2} \exp\left\{-2 \int_0^Z [\alpha_m(z) + \alpha_a(z) + \sigma_N(\lambda_2, z) N_N(z) + O_{abs}(\lambda_2, z)] dz\right\} \quad (2)$$

$$X(\lambda_3, Z) = C_3 \frac{\left[\left(\frac{\lambda_3}{\lambda_2}\right)^{-4} \beta_m(Z) + \left(\frac{\lambda_2}{\lambda_3}\right)^{-e} \beta_a(Z)\right]}{Z^2} \exp\left\{-2 \int_0^Z \left[\left(\frac{\lambda_3}{\lambda_2}\right)^{-4} \alpha_m(z) + \left(\frac{\lambda_2}{\lambda_3}\right)^{-e} \alpha_a(z) + \sigma_N(\lambda_3, z) N_N(z) + O_{abs}(\lambda_3, z)\right] dz\right\} \quad (3)$$

112 where  $X$  is the lidar signal;  $C_1$ ,  $C_2$  and  $C_3$  are lidar constants; the subscripts  $a$  and  $m$  represent  
 113 aerosol, and molecule, respectively;  $\sigma_N$  is the absorption cross section for the gas of interest;  $N_N$   
 114 is the molecular density of the gas of interest;  $O_{abs}$  is absorption of gases other than the gas of  
 115 interest and  $z$  is the altitude. The molecular density of the gas of interest can be obtained after  
 116 taking derivatives of Eq. (1), (2) and (3).

117  $\text{NO}_2$  density retrieval equation can be expressed as:

$$118 \quad N_N(Z) = \frac{\frac{1}{2} \times \frac{d}{dz} \left[ \ln \frac{X(\lambda_1, Z) X(\lambda_3, Z)}{X(\lambda_2, Z)^2} \right] - AED(z) - MED(z) - OAD(z) - B(z)}{\Delta \sigma_N} \quad (4)$$

$$119 \quad \Delta \sigma_N = 2\sigma_N(\lambda_2) - \sigma_N(\lambda_1) - \sigma_N(\lambda_3) \quad (5)$$

$$120 \quad B(z) = \frac{1}{2} \frac{d}{dz} \left[ \ln \frac{\left[\left(\frac{\lambda_3}{\lambda_2}\right)^{-4} \beta_m(Z) + \left(\frac{\lambda_2}{\lambda_3}\right)^{-e} \beta_a(Z)\right] \left[\left(\frac{\lambda_1}{\lambda_2}\right)^{-4} \beta_m(Z) + \left(\frac{\lambda_2}{\lambda_1}\right)^{-e} \beta_a(Z)\right]}{[\beta_m(Z) + \beta_a(Z)]^2} \right] \quad (6)$$

$$121 \quad AED(z) = \left[ 2 - \left(\frac{\lambda_1}{\lambda_2}\right)^{-e} - \left(\frac{\lambda_3}{\lambda_2}\right)^{-e} \right] \alpha_a(Z) \quad (7)$$

$$122 \quad MED(z) = \left[ 2 - \left(\frac{\lambda_1}{\lambda_2}\right)^{-4} - \left(\frac{\lambda_3}{\lambda_2}\right)^{-4} \right] \alpha_m(Z) \quad (8)$$

$$123 \quad OAD(z) = 2O_{abs}(\lambda_2, z) - O_{abs}(\lambda_1, z) - O_{abs}(\lambda_3, z) \quad (9)$$

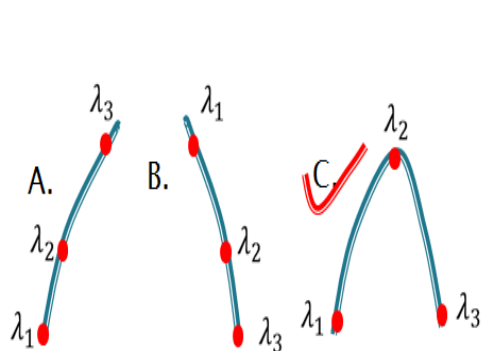
124 where  $AED$ ,  $MED$ ,  $OAD$  and  $B$  are the correction terms of aerosol extinction, molecular  
 125 extinction, absorption of gases other than the gas of interest and backscattering, respectively.  
 126 Because the atmospheric molecular density is relatively stable,  $MED$  can be corrected using a  
 127 numerical model or local real-time radiosonde data.  $OAD$  can be removed by choosing  
 128 appropriate wavelengths. However, aerosol is variable especially in PBL. For correction of  $AED$   
 129 and  $B$ , we need obtain accurate aerosol measurements. From the above  $\text{NO}_2$  retrieval relative



130 equation, how to choose the three wavelengths is very critical to improve the NO<sub>2</sub> retrievals  
 131 accuracy. We designed two rules to obtain the optimum choice for the three wavelengths:

132 **a.** The chosen three wavelengths increase differences of the NO<sub>2</sub> absorption cross section ( $\Delta\sigma_N$ )  
 133 to improve NO<sub>2</sub> retrieval.

134 According to Eq. (4), the more  $\Delta\sigma_N$  is, the less all of correction terms are. So the chosen three  
 135 wavelengths should help to increase  $\Delta\sigma_N$ . Generally, researchers only used method A  
 136 ( $\sigma_N(\lambda_1) < \sigma_N(\lambda_2) < \sigma_N(\lambda_3)$ ) or method B ( $\sigma_N(\lambda_1) > \sigma_N(\lambda_2) > \sigma_N(\lambda_3)$ ) (illustrated in Fig. 1) to choose  
 137 the three wavelengths [Liu, et al., 2017]. Equation (10) and (11) are calculated values of  $\Delta\sigma_N$  for  
 138 Method A and Method B using Eq. (5). Using Method A and B to choose the three wavelengths,  
 139 the values of  $\Delta\sigma_N$  are both decreased according to Eq. (10) and (11) compared to the  
 140 conventional two-wavelength DIAL technique. According to characteristics of the NO<sub>2</sub>  
 141 absorption spectrum showed in Fig. 2, Method C ( $\sigma_N(\lambda_1) < \sigma_N(\lambda_2) \& \sigma_N(\lambda_3) < \sigma_N(\lambda_2)$ ) is designed  
 142 to choose the three wavelengths which can increase the value of  $\Delta\sigma_N$  compared to the two-  
 143 wavelength DIAL technique according to Eq. (12).



144  
 145 Fig.1 The three-wavelength chosen methods: method A,  
 146 method B and Method C

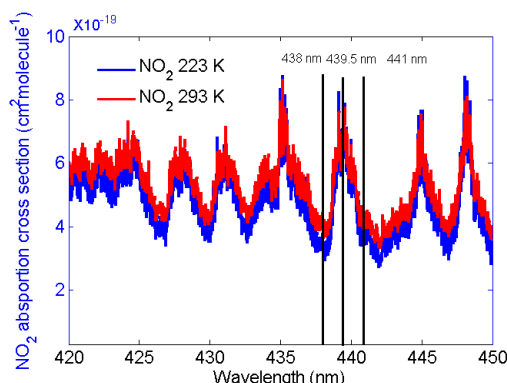


Fig.2 NO<sub>2</sub> strong absorption cross section  
 between 420 nm and 450 nm

147  
 148 Method A:  $\Delta\sigma_N = abs[\sigma_N(\lambda_2) - \sigma_N(\lambda_1)] - abs[\sigma_N(\lambda_2) - \sigma_N(\lambda_3)]$  (10)



149 Method B:  $\Delta\sigma_N = \text{abs}[\sigma_N(\lambda_2) - \sigma_N(\lambda_3)] - \text{abs}[\sigma_N(\lambda_2) - \sigma_N(\lambda_1)]$  (11)

150 Method C:  $\Delta\sigma_N = \text{abs}[\sigma_N(\lambda_2) - \sigma_N(\lambda_1)] + \text{abs}[\sigma_N(\lambda_2) - \sigma_N(\lambda_3)]$  (12)

151 **b.** The chosen three wavelengths can reduce or remove *AED*.

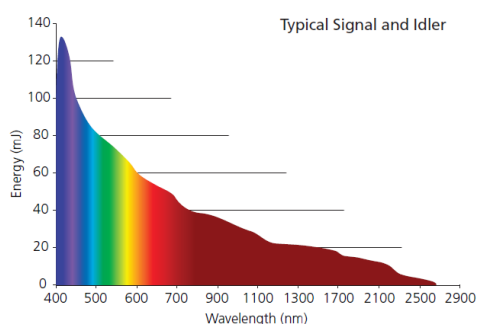
152 It means the value of *AED* is equal or close to 0. Eq. (13) is obtained from Eq. (7). Choosing the  
 153 appropriate three wavelengths to make the value of *K* in Eq. (13) equal or close to 0, the value of  
 154 *AED* will be equal or close to 0. The value of *K* in Eq. (13) changes with different aerosol  
 155 Ångström exponents. For example, to remove boundary layer aerosol influence, we can set  
 156 aerosol Ångström exponents=1 to calculate the value of *K* to choose the three wavelengths  
 157 because the size of aerosol in the boundary layer is typically large [Schuster, et al., 2006].

158  $K = 2 - \left(\frac{\lambda_1}{\lambda_2}\right)^{-e} - \left(\frac{\lambda_3}{\lambda_2}\right)^{-e}$  (13)

159

160 **3. HU three-wavelength OPO DIAL system**

Horizon performance with PL 8000 Pump



Description	
Pulsewidth (nsec)	3-7
Pointing Stability (μrad)	<±100
Linewidth (cm <sup>-1</sup> )	
Unseeded	3-7
Doubling/Mixing	<10
Energy Stability (% , 99% of shots)	<±10
Divergence (mrad, FWHM)	<2 (both axes)
Beam Diameter (mm, near field)	4-7
Beam Roundness (% , near field)	>85
Polarization (%)	
Signal Horizontal	>99
Idler Horizontal	>99

161

162 Fig.3 Continuum Horizon II energy outputs (a) and parameters (b) with PL 8000 pump

163 The HU lidar is located on the campus of HU (37.02° N, 76.34° W) in Hampton, VA. A  
 164 Continuum Horizon II tunable OPO laser and a Continuum Powerlite DLS 8000 pump laser have  
 165 recently been incorporated into HU lidar system. The OPO laser enables researchers to optimize  
 166 (tune) the wavelength choices and provides more flexibility than fixed-frequency wavelength



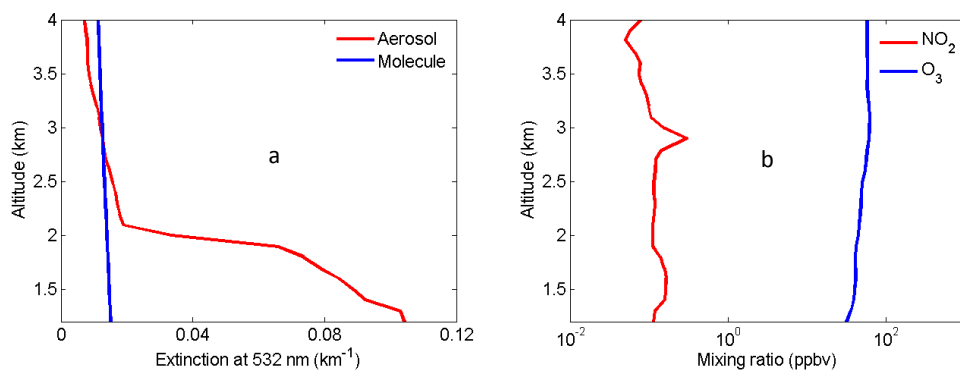


167 shifters such as Raman cells. The wavelength tuning range of our OPO extends from 192 nm to  
168 2750 nm. This range is fully automated with precision scanning for true hands-free operation.  
169 Fig. 3(a) and (b) show the Continuum Horizon II output energy and its parameters. The OPO  
170 laser energy outputs between 400 nm and 500 nm which overlap with the NO<sub>2</sub> strong absorption  
171 spectral zone in Fig. 2 produce near the maximum possible power in the spectrum. Combining  
172 the OPO laser energy outputs, NO<sub>2</sub> absorption spectral and two three-wavelength chosen rules,  
173 438 nm, 439.5 nm and 441 nm shown in Fig. 2 result in the wavelengths of HU three-wavelength  
174 DIAL system.

175 To demonstrate that the HU three-wavelength OPO DIAL system can effectively reduce aerosol  
176 influence and accurately retrieve NO<sub>2</sub>, retrieval correction terms of *AED*, *MED*, *OAD* and *B* in  
177 Eq. (4) are simulated using two-wavelength DIAL technique (438 nm and 439.5 nm) and the  
178 three-wavelength DIAL technique (438 nm, 439.5 nm and 441 nm). Ozone was used for the  
179 simulation of *OAD* because only ozone absorption can produce a little influence on NO<sub>2</sub> retrieval  
180 based on HITRAN database. Atmospheric data of aerosol, molecule, O<sub>3</sub> and NO<sub>2</sub> for these  
181 simulations are from the HU local lidar aerosol measurements, radiosonde, NASA Tropospheric  
182 Ozone Lidar Network (TOLNet) and NASA Deriving Information on Surface Conditions from  
183 Column and VERTically Resolved Observations Relevant to Air Quality (DISCOVER-AQ)  
184 measurements shown in Fig.4. Extinction and backscatter of aerosol at 438 nm, 439.5 nm and  
185 441 nm can be calculated from aerosol extinction profile at 532 nm in Fig.4 (a) with the setting  
186 of lidar ratio=50 and  $e=1, 2$  and 3. Lidar ratio is wavelength dependent and its value in the  
187 visible band is in general smaller than in the UV band for the same type of aerosols [Kuang et al.,  
188 2020; Reid et al., 2017]. Absorption of NO<sub>2</sub> and O<sub>3</sub> at 438 nm, 439.5 nm and 441 nm can be  
189 calculated using their mixing ratio profiles in Fig.4 (b) and their absorption cross-sections from

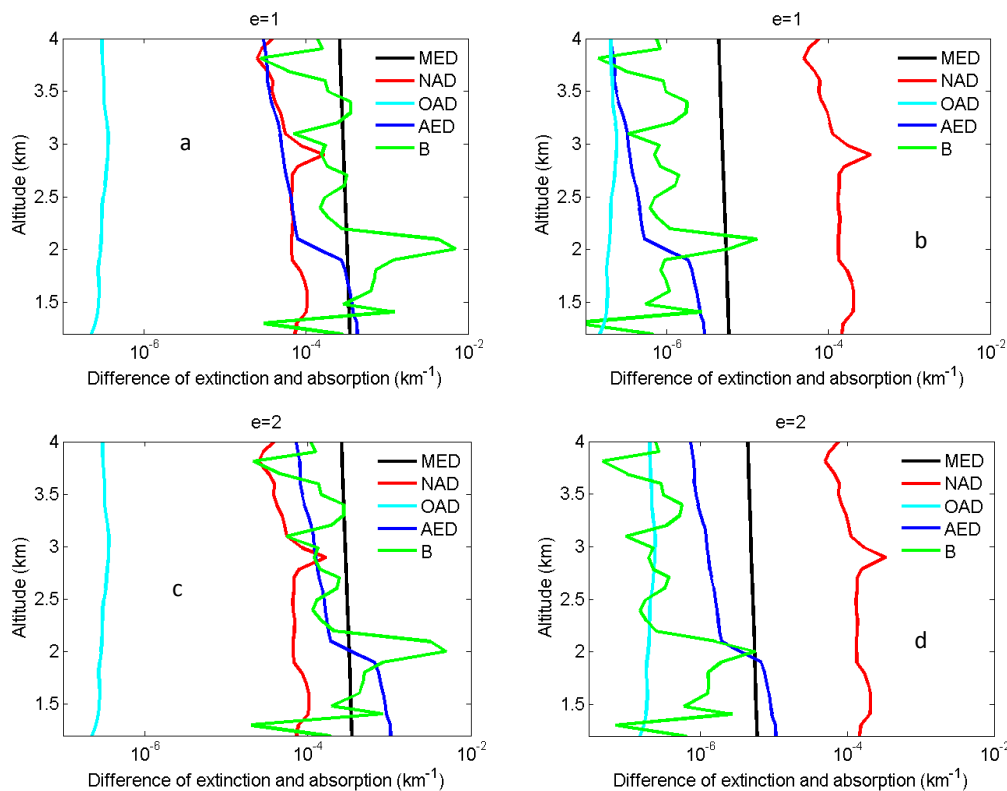


190 HITRAN database. *MED*, *AED*, *OAD*, *B* and absorption difference of  $\text{NO}_2$  (*NAD*) are simulated  
191 using two-wavelength DIAL technique with different aerosol Ångström exponents ( $e=1, 2$  and  $3$ )  
192 shown in Fig. 5 (a), (c) and (e), and the three-wavelength DIAL technique shown in Fig.5 (b), (d)  
193 and (f). In Fig. 5, red lines are *NAD*; black lines are *MED*; deep blue lines are *AED*; light blue  
194 lines are *NAD*. In Fig. 5, all *OAD* is far less than *NAD*. It is concluded that ozone absorption has  
195 negligible influence on the retrieval of  $\text{NO}_2$ . In Fig. 5 (a), (c) and (d), *MED* and *AED* in PBL are  
196 both more than *NAD* using the two-wavelength DIAL technique. Because atmospheric molecules  
197 are relatively stable, *MED* can be corrected using local model or real-time radiosonde data.  
198 However, aerosol is variable, so aerosols are a significant uncertainty for retrieving  $\text{NO}_2$  with the  
199 conventional two-wavelength DIAL technique. In Fig. 5 (b), (d) and (f), *MED* and *AED* in  
200 boundary layer are both far less than *NAD* using proposed three-wavelength DIAL technique. It  
201 is proven that three-wavelength DIAL technique can effectively decrease retrieval errors caused  
202 by aerosol extinction. From Fig.5, we can see *AED* using three-wavelength DIAL technique can  
203 be reduced to less than 2% of *AED* using two-wavelength DIAL technique at least. Therefore,  
204 even if *AED* is not corrected,  $\text{NO}_2$  still can be accurately retrieved. Moreover, simulated *B* using  
205 the two-wavelength DIAL technique and the three-wavelength DIAL technique are shown in Fig.  
206 5 with green lines. The sharp change on vertical adjacent aerosol backscatter can cause drastic  
207 changes of *B* term. In Fig. 5, the value of *B* term using three-wavelength DIAL technique is far  
208 less than using two-wavelength DIAL technique. So the three-wavelength DIAL technique can  
209 reduce more fluctuation caused by aerosol backscattering than two-wavelength DIAL technique.



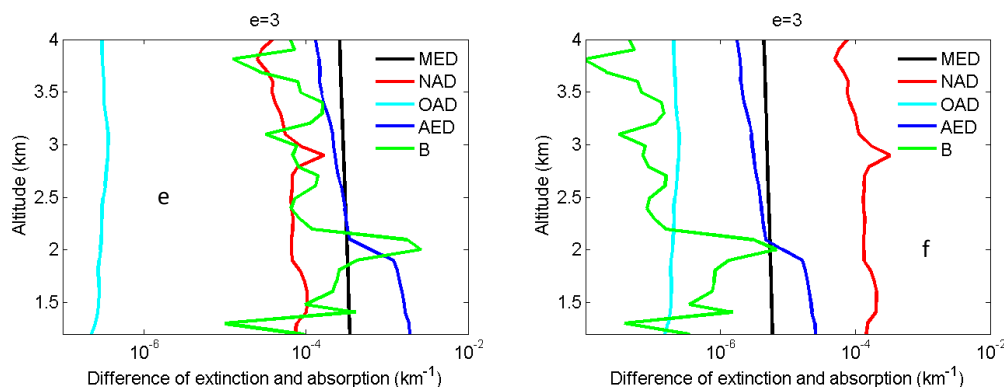
210

211 Fig.4 Atmospheric profiles used for modeling NO<sub>2</sub> lidar correction terms. (a) Aerosol extinction profile at  
 212 532 nm measured by the HU lidar and molecular extinction profile at 532 nm derived from local  
 213 radiosonde data; (b) NO<sub>2</sub> and O<sub>3</sub> mixing ratio profiles from NASA DISCOVER-AQ and TOLNet.



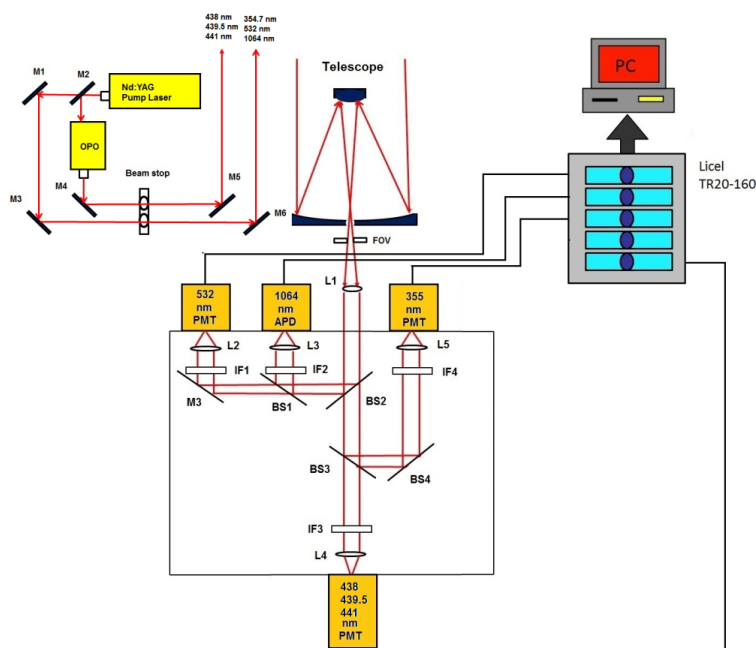
214

215



216

217 Fig.5 Simulated *MED*, *AED*, *NAD* and *OAD* using two-wavelength DIAL with (a)  $e=1$ , (c)  $e=2$  and (e)  
 218  $e=3$  and three-wavelength DIAL technique with (b)  $e=1$ , (d)  $e=2$  and (f)  $e=3$ .



219

220 Fig.6 HU lidar system (L-lens, M-mirror, BS-beam-splitter, IF-interference filter, FOV-field of view,  
 221 PMT-Photomultiplier tube, APD-Avalanche Photodetector)

222  
 223 The HU lidar system currently consists of a Continuum Horizon II tunable OPO laser and a  
 224 Continuum Powerlite DLS 8000 pump laser as the light source, a 48-inch non-coaxial  
 225 Cassegrainian-configured telescope receiver, a light separation system that uses beam splitters  
 226 and interference filters, a detecting system including photomultiplier tubes (PMT) and avalanche



227 photodiodes (APDs) and a Licel optical transient recorder. A schematic of the lidar system is  
228 shown in Fig.6. The system can be configured to measure multi-wavelength aerosols and NO<sub>2</sub>  
229 density. High-resolution (7.5 m) backscatter measurements extend from the boundary layer (1.2  
230 km) to free troposphere. The pump laser operates at three fixed wavelengths (1064, 532, and  
231 354.7 nm). The 354.7-nm laser is mostly reflected into OPO laser to produce three-wavelength  
232 (338 nm, 339.5 nm and 441 nm). Steering mirrors whose axes are aligned with a receiving  
233 telescope axis directs these laser outputs into the atmosphere. The laser backscatter is collected  
234 by a 48-inch diameter telescope and split into specific wavelength bands by a beam separation  
235 unit, which combines filters and beam-splitters for dispersion of the return backscatter to various  
236 detection channels. Using filters and beam-splitters makes the beam-splitting system simple,  
237 compact, and easy to change or add other spectral channels for other measurements. Currently,  
238 wavelengths of 438 nm, 439.5 nm, 441 nm, 354.7 nm, 532 nm and 1064 nm are focused to PMTs  
239 and APD, and recorded by a Licel data-collecting system for measurements of aerosol, and NO

#### 240 **4. Uncertainty analysis**

241 The NO<sub>2</sub> measurement uncertainty is due to several factors, and the total relative uncertainty  
242 expressed as Eq. (14) can be obtained from standard uncertainty [Leblanc et al., 2016] and Eq.  
243 (4).

$$244 \quad U_{NO_2}(z) = \sqrt{U_S(z)^2 + U_{AED}(z)^2 + U_{MED}(z)^2 + U_{OAD}(z)^2 + U_B(z)^2} \quad (14)$$

245 where  $U_{NO_2}$  is NO<sub>2</sub> total retrieval relative uncertainty using three-wavelength DIAL technique;  
246  $U_S$  is NO<sub>2</sub> retrieval relative uncertainty caused by noise of lidar signals and not discussed in this  
247 work;  $U_{MED}$ ,  $U_{OAD}$ ,  $U_{AED}$  and  $U_B$  are NO<sub>2</sub> retrieval relative uncertainty caused by molecule,  
248 absorption of gases other than the gas of interest and aerosol (extinction and backscattering)  
249 expressed as Eq. (15), (16), (17) and (18);  $u$  is uncertainty function;  $N_a$  and  $N_o$  are number



250 density (ND) of air and ozone;  $\sigma_a$  is Rayleigh scattering cross section;  $\sigma_o$  is absorption cross  
 251 section of ozone;  $S$  is lidar ratio.

$$252 \quad U_{MED}(z) = \frac{u[MED(z)]}{N_N(z)\Delta\sigma_N} = \frac{\left[2 - \left(\frac{\lambda_2}{\lambda_1}\right)^4 - \left(\frac{\lambda_2}{\lambda_3}\right)^4\right] u[\alpha_m(z)]}{N_N(z)\Delta\sigma_N} = \frac{\left[2 - \left(\frac{\lambda_2}{\lambda_1}\right)^4 - \left(\frac{\lambda_2}{\lambda_3}\right)^4\right] \sigma_a u[N_a(z)]}{N_N(z)\Delta\sigma_N} \quad (15)$$

253

$$254 \quad U_{OAD}(z) = \frac{u[OAD(z)]}{N_N(z)\Delta\sigma_N} = \frac{u[2O_{abs}(\lambda_2, z) - O_{abs}(\lambda_1, z) - O_{abs}(\lambda_3, z)]}{N_N(z)\Delta\sigma_N} = \frac{[2\sigma_o(\lambda_2, z) - \sigma_o(\lambda_1, z) - \sigma_o(\lambda_3, z)] u[N_o(z)]}{N_N(z)\Delta\sigma_N} \quad (16)$$

255

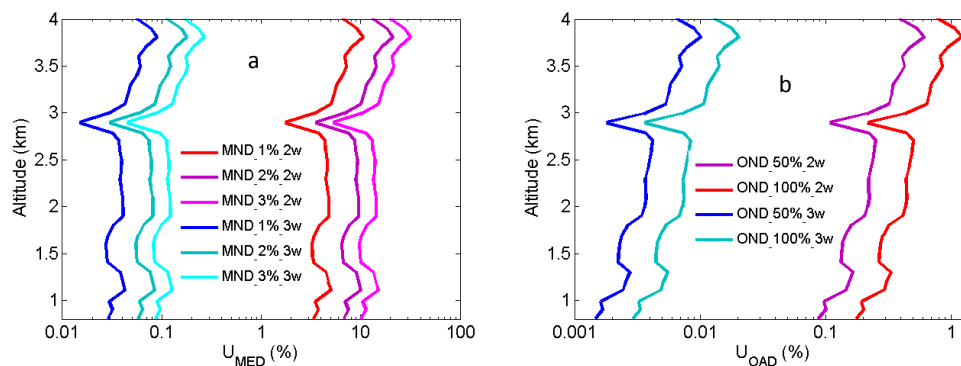
$$256 \quad U_{AED}(z) = \frac{u[AED(z)]}{N_N(z)\Delta\sigma_N} = \frac{\left[2 - \left(\frac{\lambda_2}{\lambda_1}\right)^e - \left(\frac{\lambda_2}{\lambda_3}\right)^e\right] u[\alpha_a(z, s)]}{N_N(z)\Delta\sigma_N} \quad (17)$$

$$257 \quad U_B(z) = \frac{u\left\{\frac{1}{2dz} \ln \left[ \frac{\left(\frac{\lambda_2}{\lambda_3}\right)^4 \beta_m(z) + \left(\frac{\lambda_2}{\lambda_3}\right)^e \beta_a(z, s)}{\left(\frac{\lambda_2}{\lambda_1}\right)^4 \beta_m(z) + \left(\frac{\lambda_2}{\lambda_1}\right)^e \beta_a(z, s)} \right] \right\}}{N_N(z)\Delta\sigma_N} \quad (18)$$

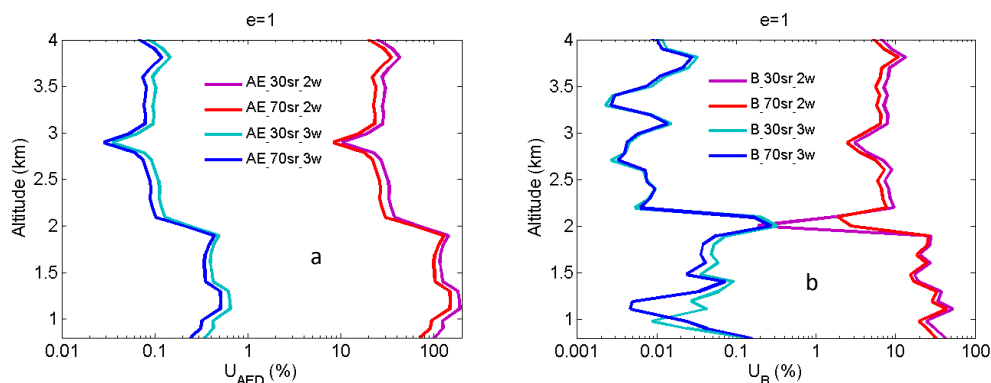
258 From Eq. (15) and (16),  $U_{MED}$  and  $U_{OAD}$  are determined by  $u[N_a(z)]$  and  $u[N_o(z)]$  (uncertainties of  
 259  $N_a$  and  $N_o$ ). In our measurements, profiles of temperature and pressure from local radiosonde are  
 260 used to calculate  $N_a$ . Usually, one radiosonde is launched for about 8-hour measurement. One  
 261 profile of air number density from local radiosonde is used to correct eight-hour  $NO_2$   
 262 measurements. According to statistics of eight-hour variation of temperature and pressure in  
 263 local four seasons, the uncertainty of  $N_a$  is between 1% and 3%.  $U_{MED}$  using two-wavelength  
 264 DIAL technique and the three-wavelength DIAL technique are calculated according to Eq. (15)  
 265 with the uncertainty of  $N_a$  as 1%, 2% and 3% shown in Fig. 7(a).  $U_{MED}$  using three-wavelength  
 266 DIAL technique is far less than using two-wavelength DIAL technique.  $N_o$  is obtained from local  
 267 measurements. Because of very low values of ozone absorption cross section differentials, with  
 268 the uncertainty of  $N_o$  as 50% and 100%,  $U_{OAD}$  using two-wavelength DIAL technique and using  
 269 the three-wavelength DIAL technique are both less 0.5% from Fig.7 (b). Ozone absorption  
 270 correction is neglect in  $NO_2$  retrieval. From Eq. (17) and (18),  $U_{AED}$  and  $U_B$  are determined by



271 uncertainties of  $a_a$ ,  $\beta_a$  and  $e$ . For HU lidar system, 532-nm elastic signals are used to calculate  $a_a$   
272 and  $\beta_a$  with Fernald method to correct  $\text{NO}_2$  retrieval. 50 sr is usually chosen as lidar ratio to  
273 retrieve  $a_a$  and  $\beta_a$ . The lidar ratio is variable, so uncertainties of  $a_a$  and  $\beta_a$  are caused by chosen  
274 lidar ratio. The range of lidar ratio is about from 30 sr to 70 sr for 532 nm. The uncertainty of  
275 lidar ratio is 40% for 50 sr. The uncertainties of  $a_a$  and  $\beta_a$  are calculated with uncertainty of lidar  
276 ratio as 40%. Finally,  $U_{AED}$  and  $U_B$  using two-wavelength DIAL technique and using the three-  
277 wavelength DIAL technique are calculated with the Ångström exponent as 1, 2 and 3 shown in  
278 Fig. 8, 9 and 10. From these figures,  $U_{AED}$  and  $U_B$  using three-wavelength DIAL technique are  
279 both less 4%. However,  $U_{AED}$  below 2 km using two-wavelength DIAL technique are more than  
280 90% after correction of aerosol extinction. Moreover,  $\text{NO}_2$  number density total relative  
281 uncertainty except  $U_s$  with Ångström exponent as 1, 2 and 3 are calculated shown in Fig. 11(a),  
282 (b) and (c).



283  
284 Fig.7  $\text{NO}_2$  number density relative uncertainty owing to air number density (a) and ozone number density  
285 (b).

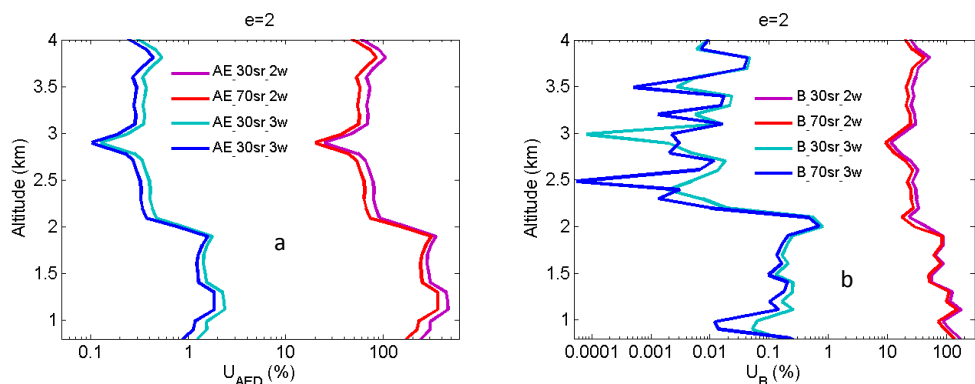


286

287 Fig.8 NO<sub>2</sub> number density relative uncertainty owing to aerosol extinction (a) and backscatter (b) with e=

288 1.

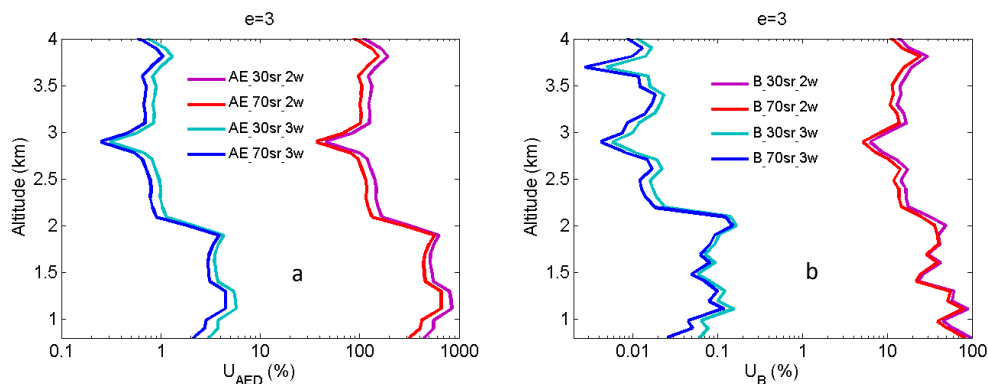
289



290

291 Fig.9 NO<sub>2</sub> number density relative uncertainty owing to aerosol extinction (a) and backscatter (b) with e=

292 2.



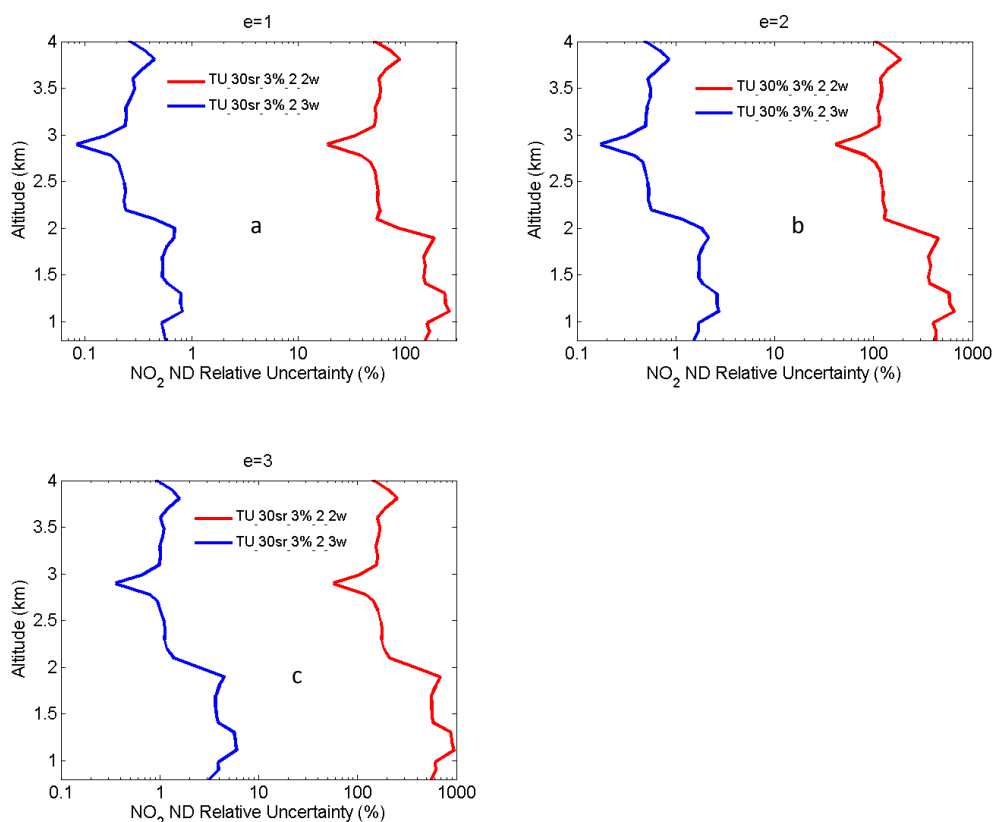
293

294 Fig.10 NO<sub>2</sub> number density relative uncertainty owing to aerosol extinction (a) and backscatter (b) with

295 e=3.

296





297

298

299

300 Fig.11 NO<sub>2</sub> number density total relative uncertainty except  $U_s$  with  $e=1$  (a),  $e=2$  (b) and  $e=3$  (c).

301

## 302 5. Results

303 The three-wavelength DIAL technique was implemented by the HU lidar measurements during

304 two cases at night and the resulting vertical profiles are presented in Fig. 12. All NO<sub>2</sub> lidar

305 measurements presented here are obtained at times with less than 10% cloud coverage below 8

306 km. HU lidar 438 nm (blue line), 439.5 nm (red line) and 441 nm (black line) elastic signals

307 measured at 21:00 (local time) on May 13, 2020 and 22:00 (local time) on July 27, 2020 are

308 shown in Fig. 12 (a) and (c), respectively. The average integration time for these signals is 2

309 minutes. Determined from the lidar elastic signals in Fig. 8 (a) and (c), there is an existing

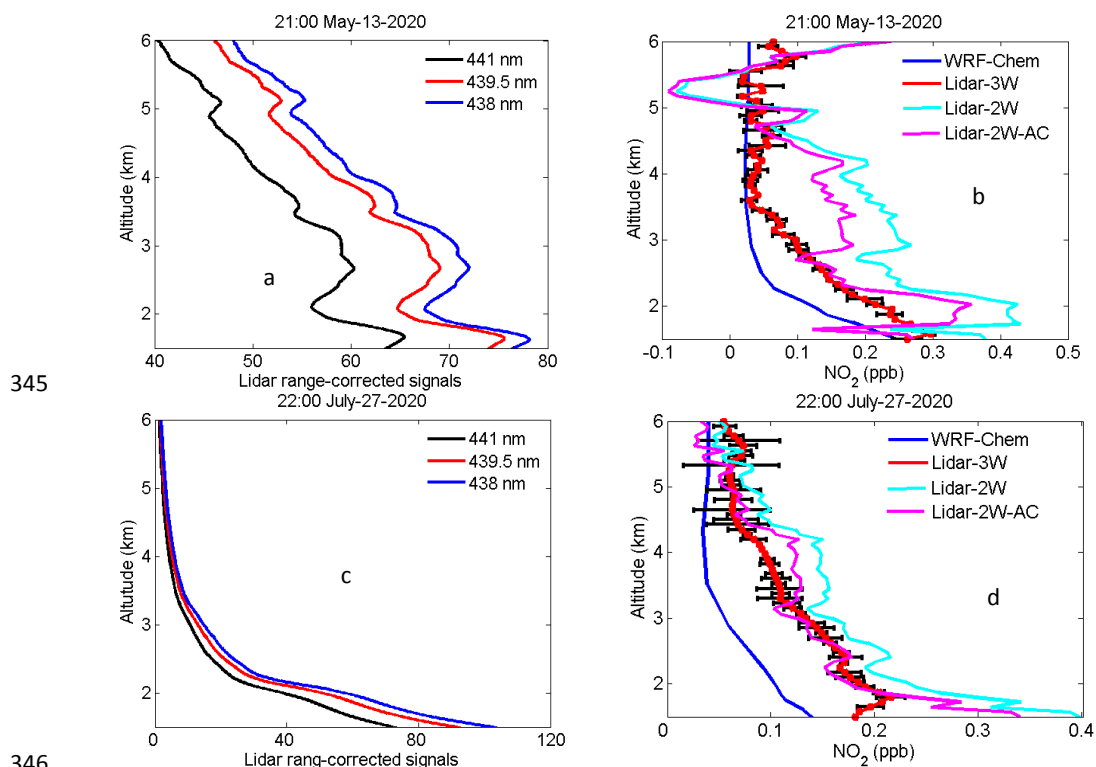
310 aerosol layer between 2.2 km and 3.5 km on May 13, while July 27 presented a clean atmosphere.



311 Fig. 12 (b) and (d) show retrieved NO<sub>2</sub> profiles using the three-wavelength DIAL technique (red  
312 line). In Fig. 12 (b), the retrieved NO<sub>2</sub> profile between 2.2 km and 3.5 km on May 13 is smooth  
313 and not affected by the aerosol layer. The NO<sub>2</sub> profiles (sky-blue line and purple line) were also  
314 retrieved using the conventional two-wavelength DIAL technique without and with aerosol  
315 correction shown in Fig. 12 (b) resulting in a bump between 2.2 km and 3.5 km in the NO<sub>2</sub>  
316 profile retrieved using the two-wavelength DIAL technique. This inconsistency suggests that the  
317 two-wavelength DIAL technique cannot remove AED of the aerosol layer between 2.2 km and  
318 3.5 km and the retrieved NO<sub>2</sub> profile contains AED interference. Moreover, the NO<sub>2</sub> retrievals  
319 below 2 km using two-wavelength DIAL technique shown in Fig. 12 (b) and (d) are more than  
320 the three-wavelength DIAL technique suggesting that the AED of boundary aerosol was not  
321 correctly removed. Aerosol correction is very important for NO<sub>2</sub> retrieval using the conventional  
322 two-wavelength DIAL technique [Browell et al., 1985]. These results suggest that the proposed  
323 three-wavelength DIAL technique can effectively remove influence of aerosol on the retrieval of  
324 NO<sub>2</sub>. As a first-order assessment of the HU lidar NO<sub>2</sub> profiles, we compare the retrieval results to  
325 simulated data from the Weather Research and Forecasting Chemistry (WRF-Chem) model  
326 (Grell et al., 2005) at 12 km × 12 km spatial resolution. Past studies have demonstrated that  
327 WRF-Chem simulated NO<sub>2</sub> results show good agreement between the OMI and aircraft  
328 measurements [Amnuaylojaroen et al., 2019; Barten et al., 2020] providing a data source to  
329 examine the accuracy of the HU retrievals using both two-wavelength DIAL technique and  
330 three-wavelength DIAL technique. The HU local NO<sub>2</sub> profiles for these two cases are simulated  
331 using WRF-Chem model and shown in Fig. 12 (b) and (d). WRF-Chem simulated NO<sub>2</sub>  
332 magnitudes tend to be lower compared to HU retrieved NO<sub>2</sub> profiles using three-wavelength  
333 DIAL technique (typically within ±0.1 ppb), except above 3.5 km on May 13, 2020, however,



334 the comparison demonstrates a consistent vertical profile shape between observations and the  
335 model simulation. And retrieval results using the three-wavelength DIAL technique are much  
336 closer to simulated values compared to using the two-wavelength DIAL technique. These figures  
337 also demonstrate that the reduced fluctuations caused by aerosol backscatter when using the  
338 three-wavelength DIAL technique results in vertical profiles of  $\text{NO}_2$  which are much more  
339 consistent with simulated data when compared to results of the two-wavelength DIAL retrievals.  
340 Both the WRF-Chem simulated profiles and the HU retrievals of  $\text{NO}_2$  using three-wavelength  
341 DIAL technique are associated with uncertainties which could result in the differences in  
342 magnitude; however, given the consistent nature in the vertical profile shapes from both data  
343 sources provides confidence that the HU lidar is retrieving  $\text{NO}_2$  vertical profiles using three-  
344 wavelength DIAL technique in the troposphere.





347 Fig.12 HU lidar 438 nm, 439.5 nm and 441 nm elastic signals measured at 21:00 (local time) on May 13,  
348 2020 (a) and 22:00 (local time) on July 27, 2020 (c); NO<sub>2</sub> profiles obtained using three-wavelength DIAL  
349 technique, two-wavelength DIAL technique and WRF-Chem model at 21:00 on May 13, 2020 (b) and  
350 22:00 on July 27, 2020 (d).  
351

## 352 **6. Conclusion**

353 This study describes a lidar retrieval technique using three wavelengths simultaneously emitted  
354 from an OPO laser to measure tropospheric NO<sub>2</sub> profiles. The three-wavelength DIAL retrieval  
355 equations describe how the retrievals decrease errors caused by aerosol interference. Aerosol  
356 extinction differences using this proposed technique can be decreased to less than 2% of aerosol  
357 extinction differences resulting from a conventional two-wavelength DIAL technique.  
358 Comparing the HU lidar results to WRF-Chem model output demonstrates that the NO<sub>2</sub>  
359 magnitudes and vertical structure are in much better agreement with simulated data when  
360 applying the three-wavelength DIAL technique compared to using the two-wavelength technique.  
361 In the future, we will add new filters to obtain daytime NO<sub>2</sub> measurements. We also plan to  
362 purchase NO<sub>2</sub> balloonsondes for acquiring true validation data to evaluate HU lidar NO<sub>2</sub> results.

363

## 364 **Acknowledgments**

365 We thank NASA TOLNet and NASA DISCOVER-AQ measurements for our simulation work.  
366 This study was supported by the PIRT project funded by US Army Research, Development and  
367 Engineering Command (AQC) Center (DOD) under HU PIRT Award # 551150-211150) and the  
368 National Oceanic and Atmospheric Administration- Cooperative Science Center for Earth  
369 System and Sciences and Remote Sensing Technologies (NOAA-CESSRST) under the  
370 Cooperative Agreement Grant #: NA16SEC4810008. The statements contained within the  
371 manuscript/research article are not the opinions of the funding agency or the U.S. government,  
372 but reflect the author's opinions. HU lidar data are available at <http://cas.hamptonu.edu/data->



373 [products/](#). Matthew Johnson's contribution was supported by the NASA's TOLNet Science  
374 Team and the Tropospheric Composition Program. We also thank Dr. Gabriele Pfister from the  
375 Atmospheric Chemistry Observations & Modeling Lab at the National Center for Atmospheric  
376 Research for providing the WRF-Chem calculation applied in this study.

377 **Reference:**

378 Amnuaylojaroen T., Macatangay R.C., and Khodmanee S.: Modeling the effect of VOCs from  
379 biomass burning emissions on ozone pollution in upper Southeast Asia, *Heliyon.*, 5(10), e02661.  
380 Published 2019 Oct 17. doi:10.1016/j.heliyon.2019.e02661, 2019.

381 Barten, J. G. M., Ganzeveld, L. N., and Visser, A. J.: Rodrigo Jiménez, and Maarten C.Krol,  
382 Evaluation of nitrogen oxides (NO<sub>x</sub>) sources and sinks and ozone production in Colombia and  
383 surrounding areas, *Atmos. Chem. Phys.*, 20, 9441–9458, 2020.

384 Beirle, S., Boersma, K., Platt, U., Lawrence, M., and Wagner, T.: Megacity Emissions and  
385 Lifetimes of Nitrogen Oxides Probed from Space, *Science.*, 333, 1737–1739, 2011.

386 Beirle, S., Platt, U., Wenig, M., and Wagner, T.: Weekly cycle of NO<sub>2</sub> by GOME measurements:  
387 a signature of anthropogenic sources, *Atmos. Chem. Phys.*, 3(6), 2225–2232, 2003.

388 Berg, N., Mellqvist, J., Jalkanen, J. P., and Balzani, J.: Ship emissions of SO<sub>2</sub> and NO<sub>2</sub>: DOAS  
389 measurements from airborne platforms, *Atmos. Meas. Tech.*, 5(5), 1085–1098, 2012.

390 Berglund, M., Boström, C. E., Bylin, G., Ewetz, L., Gustafsson, L., Moldéus, P., Norberg, S.,  
391 Pershagen, G., and Victorin, K.: Health risk evaluation of nitrogen oxides, *Scandinavian journal*  
392 *of work: environment and health.*, 19, 1993.

393 Bertram, T. H., Heckel, A., Richter, A., Burrows, J. P., and Cohen, R. C.: Satellite measurements  
394 of daily variations in soil NO<sub>x</sub> emissions, *Geophys. Res. Lett.*, 32, L24812, 2005.

395 Boersma, K. F., Jacob, D. J., Eskes, H. J., Pinder, R. W., Wang, J., and Van Der A, R. J.:  
396 Intercomparison of SCIAMACHY and OMI tropospheric NO<sub>2</sub> columns: Observing the diurnal  
397 evolution of chemistry and emissions from space, *J. Geophys. Res.*, 113, D16S26, 2008.

398 Bovensmann, H., Burrows, J. P., Buchwitz, M., Frerick, J., Noel, S., Rozanov, V. V., Chance, K.  
399 V., and Goede, A. P. H.: SCIAMACHY: Mission objectives and measurement modes, *J. Atmos.*  
400 *Sci.*, 56(2), 127–150, 1999.



- 401 Bucsela, E. J., et al.: Comparison of tropospheric NO<sub>2</sub> in situ aircraft measurements with near-  
402 real-time and standard product data from the Ozone Monitoring Instrument, *J. Geophys. Res.*,  
403 113, D16S31, doi:10.1029/2007JD008838, 2008.
- 404 Celarier, E. A., et al.: Validation of Ozone Monitoring Instrument nitrogen dioxide columns, *J.*  
405 *Geophys. Res.*, 113, D15S15, doi:10.1029/2007JD008908, 2008.
- 406 Chen, Y., Jie Wang, Huang, J., and Hu, Shunxing. (2017). Measurement of atmospheric NO<sub>2</sub>  
407 profile using three-wavelength dual-differential absorption lidar, *Proc. SPIE.*, 10605, 106053L,  
408 2017.
- 409 Cui, Y. Z., J. Lin, T., Song, C. Q., Liu, M. Y., Yan, Y. Y., Xu, Y., and Huang, B.: Rapid growth  
410 in nitrogen dioxide pollution over Western China 2005-2013, *Atmos. Chem. Phys.*, 16(10), 2016.
- 411 Edward V. B., Syed I., and Scott T. S.: Ultraviolet DIAL measurements of O<sub>3</sub> profiles in regions  
412 of spatially inhomogeneous aerosols, *Appl. Opt.*, 24, 2827-2836, 1985.
- 413 Fredriksson, K. A. and Hertz, H. M.: Evaluation of the DIAL technique for studies on NO<sub>2</sub>  
414 using a mobile lidarsystem, *Appl. Opt.*, 23(9), 1403–1411, 1984.
- 415 Herman, J., Cede, A., Spinei, E., Mount, G., Tzortziou, M., and Abuhassan, N.: NO<sub>2</sub> column  
416 amounts from ground-based Pandora and DOAS spectrometers using the direct-sun DOAS  
417 technique: Intercomparisons and application to OMI validation, *J. Geophys. Res.*, 114(D13),  
418 2009.
- 419 Kollonige, D. E., Thompson, A. M., Josipovic, M., Tzortziou, M., Beukes, J. P., Burger, R.,  
420 Martins, D. K., van Zyl, P. G., Vakkari, V., and Laakso, L.: OMI satellite and ground - based  
421 Pandora observations and their application to surface NO<sub>2</sub> estimations at terrestrial and marine  
422 sites, *Journal of Geophysical Research.*, 123, 1441– 1459, 2018.
- 423 Kuang, S., M. J. Newchurch, J. Burris, and X. Liu (2013), Ground-based lidar for atmospheric  
424 boundary layer ozone measurements, *Appl. Opt.*, 52, 3557-3566,  
425 <http://dx.doi.org/10.1364/AO.52.003557>.
- 426 Kuang, S., Wang, B., Newchurch, M. J., Knupp, K., Tucker, P., Eloranta, E. W., Garcia, J. P.,  
427 Razenkov, I., Sullivan, J. T., Berkoff, T. A., Gronoff, G., Lei, L., Senff, C. J., Langford, A. O.,  
428 Leblanc, T., and Natraj, V.: Evaluation of UV aerosol retrievals from an ozone lidar, *Atmos.*  
429 *Meas. Tech.*, 13, 5277–5292, <https://doi.org/10.5194/amt-13-5277-2020>, 2020.
- 430 Lamsal, L. N., et al.: Evaluation of OMI operational standard NO<sub>2</sub> column retrievals using in situ  
431 and surface - based NO<sub>2</sub> observations, *Atmos. Chem. Phys.*, 14, 11,587 - 11,609, 2014.



- 432 Larkin, A., Geddes, J. A., Martin, R. V., Xiao, Q., Liu, Y., Marshall, J. D., Brauer, M., and  
433 Hystad, P.: Global Land Use Regression Model for Nitrogen Dioxide Air Pollution.  
434 *Environmental Science and Technology.*, 51(12), 6957-6964, 2017.
- 435 Leblanc, T., Sica, R. J., van Gijssel, J. A. E., Godin-Beekmann, S., Haeefe, A., Trickl, T., Payen,  
436 G., and Liberti, G.: Proposed standardized definitions for vertical resolution and uncertainty in  
437 the NDACC lidar ozone and temperature algorithms – Part 2: Ozone DIAL uncertainty budget,  
438 *Atmos. Meas. Tech.*, 9, 4051–4078, <https://doi.org/10.5194/amt-9-4051-2016>, 2016.
- 439 Li, Z., Guo, J., Ding, A., Liao, H., Liu, J., Sun Y., Wang, T., Xue, H., Zhang, H., and Zhu, B.:  
440 Aerosol and boundary-layer interactions and impact on air quality, *National Science Review.*,  
441 4( 6), 2017.
- 442 Liang, M., Guan, P., &Zheng, K.: Remote sensing of atmospheric NO<sub>2</sub> by employing the  
443 continuous-wave differential absorption lidar technique, *Opt. Express.*, 25, A953-A962, 2017.
- 444 Newchurch, M. J., Ayoub, M. A., Oltmans, S., Johnson, B., and Schmidlin, F. J.: Vertical  
445 distribution of ozone at four sites in the United States, *J. Geophys. Res.*, 108(D1), 4031, 2003.
- 446 Reid, J. S., R. E. Kuehn, R. E. Holz, E. W. Eloranta, K. C. Kaku, S. Kuang, M.J. Newchurch, A.  
447 M. Thompson, C. R. Trepte, J. Zhang, S. A. Atwood, J. L. Hand, B. N. Holben, P. Minnis, D. J.  
448 Posselt (2017), Ground based high spectral resolution lidar observation of aerosol vertical  
449 distribution in the summertime Southeast United States, *J. Geophys. Res. Atmos.*, 122(2), 2970-  
450 3004, doi:[10.1002/2016JD025798](https://doi.org/10.1002/2016JD025798).
- 451 Rothe, K. W., Brinkmann, U., and Walther, H.: Applications of tunable dye lasers to air pollution  
452 detection: measurements of atmospheric NO<sub>2</sub> concentrations by differential absorption, *Appl.*  
453 *Phys.*, 3(2), 1974.
- 454 Russell, A. R., Valin, L. C., and Cohen, R. C.: Trends in OMI NO<sub>2</sub> observations over the United  
455 States: effects of emission control technology and the economic recession, *Atmos. Chem, Phys.*,  
456 12, 12197–12209, <https://doi.org/10.5194/acp-12-12197-2012>, 2012.
- 457 Schuster, G., Dubovik, O., and Holben, B. N.: Ångström exponent and bimodal aerosol size  
458 distributions, *J. Geophys. Res.*, 111, D07207, 2006.
- 459 Scott, D. C., Herman, R. L., Webster, C. R., May, R. D., Flesch, G. J., and Moyer, E. J.:  
460 Airborne Laser Infrared Absorption Spectrometer (ALIAS-II) for in situ atmospheric  
461 measurements of N<sub>2</sub>O, CH<sub>4</sub>, CO, HCL, and NO<sub>2</sub> from balloon or remotely piloted aircraft  
462 platforms, *Appl. Opt.*, 38, 4609-4622, 1999.



- 463 Sullivan, J., Rabenhorst, S. D., Dreessen, J., McGee, T. J., Delgado, R., Twigg, L., and Sumnicht,  
464 G.: Lidar observations revealing transport of O<sub>3</sub> in the presence of a nocturnal low-level jet:  
465 Regional implications for "next-day" pollution, *Atmospheric Environment*, 158, 160-171, 2017.
- 466 Sullivan, J., McGee, T. J., Sumnicht, G. K., Twigg, L. W., and Hoff, R. M.: A mobile differential  
467 absorption lidar to measure sub-hourly fluctuation of tropospheric ozone profiles in the  
468 Baltimore–Washington, D.C. region, *Atmos. Meas. Tech.*, 7, 3529–3548, 2014.
- 469 Sunesson, J. A.: Differential absorption lidar system for routine monitoring of tropospheric  
470 ozone, *Appl. Opt.*, 33(30), 7045-7058, 1994.
- 471 U.S. EPA 2016. Climate change indicators in the United States, 2016. Fourth edition. EPA 430-  
472 R-16-004.
- 473 U.S. EPA 2018. Data from the Air Pollutant Emission Trends Data website. Accessed 2018.  
474 <https://www.epa.gov/air-emissions-inventories/air-pollutant-emissions-trends-data>.
- 475 Valks, P., Pinardi, G., Richter, A., Lambert, J. C., Hao, N., Loyola, D., Van Roozendael, M., and  
476 Emmadi, S.: Operational total and tropospheric NO<sub>2</sub> column retrieval for GOME-2, *Atmos.*  
477 *Meas. Tech.*, 4(7), 1491–1514, 2011.
- 478 Volten, H., Brinksma, E. J., Berkhout, A. J. C., Hains, J., Bergwerff, J. B., Van der Hoff, G.  
479 R., Apituley, A., Dirksen, R. J., Calabretta, J. S., and Swart, D. P. J.: NO<sub>2</sub> lidar profile  
480 measurements for satellite interpretation and validation, *Journal of Geophysical Research.*,  
481 114(24), 2009.
- 482 Weibring, P., Smith, J. N., Edner, H., & Svanberg, S.: Development and testing of a frequency-  
483 agile optical parametric oscillator system for differential absorption lidar, *Review of Scientific*  
484 *Instruments.*, 74, 4478, 2003.